

# Influence of laser powder bed fusion process parameters on the microstructure of solution heat-treated nickel-based superalloy Alloy 247LC

Olutayo Adegoke<sup>a,\*</sup>, Satyanarayana Rao Polisetti<sup>a</sup>, Jinghao Xu<sup>b</sup>, Joel Andersson<sup>a</sup>, Håkan Brodin<sup>c</sup>, Robert Pederson<sup>a</sup>, Peter Harlin<sup>a,d</sup>

<sup>a</sup> University West, Department of Engineering Science, SE-46186 Trollhättan, Sweden

<sup>b</sup> Linköping University, Department of Management and Engineering, SE-58183 Linköping, Sweden

<sup>c</sup> Siemens Industrial Turbomachinery, Finspång, Sweden

<sup>d</sup> Sandvik Additive Manufacturing, Sandviken, Sweden

## ARTICLE INFO

### Keywords:

Laser powder bed fusion  
Nickel-based superalloy  
Alloy 247  
Heat treatment  
Grain structure  
Recrystallization  
Dislocation density  
Gamma prime  
Microsegregation  
Design of experiment

## ABSTRACT

In this study, Alloy 247LC samples were built with different laser powder bed fusion (L-PBF) process parameters. The samples were then subjected to solution heat treatment at 1260 °C for 2 h. The grain size of all the samples increased significantly after the heat treatment. The relationship between the process parameters and grain size of the samples was investigated by performing a design of experiment analysis. The results indicated that the laser power was the most significant process parameter that influenced the grain height and aspect ratio. The laser power also significantly influenced the grain width. The as-built and as-built + heat-treated samples with high, medium, and low energy densities were characterized using a field emission gun scanning electron microscope equipped with an electron backscatter diffraction detector. The micrographs revealed that the cells present in the as-built samples disappeared after the heat treatment. Isolated cases of twinning were observed in the grains of the as-built + heat-treated samples. The disappearance of cells, increase in the grain size, and appearance of twins suggested that recrystallization occurred in the alloy after the heat treatment. The occurrence of recrystallization was confirmed by analyzing the grain orientation spread of the alloy, which was lower and more predominantly <1° in the as-built + heat-treated conditions than in the as-built conditions. The microhardness of the as-built + heat-treated samples were high which was plausible because γ' precipitates were observed in the samples. However, the L-PBF process parameters had a very low correlation with the microhardness of the as-built + heat-treated samples.

## 1. Introduction

Alloy 247LC is strengthened by the precipitation of the γ' precipitate in the γ matrix [1]. The high-volume fraction and optimal size of the γ' precipitate endow the superalloy with high creep strength. The superalloy also shows adequate fatigue, corrosion, and oxidation resistance at high temperatures. Hence, it can be used in the hot section of gas turbines where the temperature is high (approximately 1200–1370 °C) and the environment is highly corrosive [1]. Recently, the printability of Alloy 247LC by laser powder bed fusion (L-PBF) has been investigated [2–11]. The major challenge in printing Alloy 247LC is solidification cracking, which is promoted by their large solidification temperature

range and high plastic strains induced by the L-PBF process [2]. The L-PBF process parameters influence the microstructure including the formation of cracks. Carter et al. [12] investigated the influence of the L-PBF process parameters on the crack and void content of CMSX 486. The study revealed that the L-PBF process parameters, for example the laser power and scanning speed, significantly influenced the crack and void contents in the alloy. In another study, Thomas et al. [13] calculated a normalized volumetric energy density  $E^*$  for additive manufactured alloys according to Eq. (1).

$$E^* = q^*/(v \cdot l) = [Aq/(2v \cdot l)] [1/0.67\rho C_p(T_m - T_0)] \quad (1)$$

where  $q$  is the laser power,  $v$  is the scanning speed and  $l$  is the layer

\* Corresponding author.

E-mail address: [olutayo.adegoke@hv.se](mailto:olutayo.adegoke@hv.se) (O. Adegoke).

<https://doi.org/10.1016/j.matchar.2021.111612>

Received 10 September 2021; Received in revised form 14 November 2021; Accepted 20 November 2021

Available online 26 November 2021

1044-5803/© 2021 The Authors. Published by Elsevier Inc. This is an open access article under the CC BY license (<http://creativecommons.org/licenses/by/4.0/>).

thickness (the normalized values are  $q^*$ ,  $v^*$  and  $l^*$  respectively).  $A$  is the surface absorptivity,  $r$  is the beam radius,  $T_m$  and  $T_0$  are the melting and initial temperature of the material respectively.  $C_p$  is the specific heat capacity and  $\rho$  is the density. The study plotted a process map of the alloys (including Alloy 247LC). At certain  $1/h^*$  values ( $h^*$  is the normalized hatch distance), Alloy 247LC with low values of  $E^*$  below a threshold value (approximately 2.5) produced voids. High values of  $E^*$ , above a threshold value (approximately 13) produced solidification cracks. In addition to the process parameters named above, the scanning strategy utilized in the L-PBF process influence the microstructure. This was revealed by Carter et al. [14] in a study that investigated the effect of a scanning strategy called island scanning on the microstructure of L-PBF Alloy 247LC. The island scanning and its associated heating pattern produced regions of fine grains which were at the boundaries of columnar grains. These fine grains had large misorientation angles that promoted cracking. A post-build heat treatment, such as hot isostatic pressing (HIP) (to close the internal pores and cracks), solution + aging is usually required to achieve the desired final properties [9]. Generally, in nickel-based superalloys, the solution heat treatment is followed by a aging heat treatment to precipitate  $\gamma'$  with an optimum size and morphology in order to achieve good creep properties [1]. The heat treatment also homogenizes the microstructure. Homogenization is required because the as-built alloy microstructure contains eutectic microconstituents and shows element segregation, which can cause incipient melting. This may, in turn, limit the ability of the microstructure to attain complete solutioning before aging [1]. The grain structure and size of the heat-treated microstructure are known to influence the creep properties of the alloy, where the poor ductility in the grain boundaries promotes failure [1]. Thus, directionally solidified (DS) parts, which have fewer grain boundaries than their polycrystalline counterparts, offer improved creep resistance [15]. The columnar grains in alloys prepared using L-PBF, aligned in the  $\langle 001 \rangle$  build direction, resemble DS parts, and thus may be beneficial for improving the creep resistance when their grain size is optimally large, and they are aligned parallel to the loading direction. This large grain size is particularly required for good creep resistance in the high-temperature applications of Alloy 247LC [5]. This concept was demonstrated in the study by Hilal et al. [16] where the creep resistance of L-PBF Alloy 247LC sample built at  $90^\circ$  orientation was compared to an equivalent sample built at  $30^\circ$  orientation. The result showed that the  $90^\circ$  orientation produced better creep resistance than the  $30^\circ$  orientation. The high creep resistance in the  $90^\circ$  sample was attributed to its large columnar grains while the low creep resistance in the  $30^\circ$  sample was attributed to its small equiaxed grains. In fact, single crystal alloys are preferred for high-temperature applications. It has been recently demonstrated that single crystals can be printed using the electron beam powder bed fusion technique [17]. In the present study, the authors investigated the effect of the process parameters on the grain structure, size, and texture of the Alloy 247LC. The plastic strain and the resulting stored energy are the driving forces for recrystallization, which is followed by the grain growth [18]. It has already been mentioned that high plastic strain is generated in the L-PBF process, which may promote recrystallization [19]. The recrystallization process is also influenced by the texture, grain size, grain orientation, and temperature [18]. The presence of secondary phase constituents, such as carbides, may inhibit the grain growth [20]. Thus, further studies are required in this regard to learn how to create a microstructure that results in the desired properties of the end-application with focus on optimizing properties like creep.

The as-built microstructure of the Alloy 247LC has been reported by Wang et al. [10] and Divya et al. [11]. It consists of small columnar grains that are epitaxially solidified from the substrate or previously melted layer of powder. The grains grow parallel to the build direction and the resulting texture is strong in the  $\langle 001 \rangle$  direction and contain sub-micron-sized cells with a high dislocation density [10]. The  $\gamma$ ,  $\gamma'$ ,  $\gamma/\gamma'$  eutectic, and carbide phases are present in the microstructure, and Hf, Ta, Al, Ti, and Cr segregate to the cell boundaries. The

microstructure of the L-PBF-printed Alloy 247LC after heat treatments has been investigated. Boswell et al. [21] found that solid-state cracking, which is either strain-age cracking or ductility dip cracking, occurred during a post-processing heat treatment performed for 2 h [21]. Strain age cracking occurred in the samples heat-treated above  $750^\circ\text{C}$  and was caused by the known interaction of the high residual stresses and  $\gamma'$  precipitation. Moreno et al. [22] studied the microstructure of Alloy 247LC subjected to different solution heat treatments but aged at a constant temperature. It was found that only recovery occurred below  $1230^\circ\text{C}$ , whereas recrystallization and grain growth occurred above  $1230^\circ\text{C}$ . At  $1230^\circ\text{C}$ , some recrystallized grains could be detected, although most of the grains did not recrystallize. Above  $1230^\circ\text{C}$ , the grains showed reduced texture and anisotropy as compared to the grains observed below  $1230^\circ\text{C}$ . The inability of the alloy to recrystallize below  $1230^\circ\text{C}$  (recrystallization occurred at  $1260^\circ\text{C}$ ) was also observed by Xu [23]. Xu proposed that the recrystallization of L-PBF Alloy 247LC occurs above the solvus temperature of  $\gamma'$ , owing to the absence of Zener pinning effect generated by the grain boundary  $\gamma'$  precipitates. In a previous study [11], the recrystallization of an L-PBF-printed Alloy 247LC was investigated after a solution heat treatment at  $1230^\circ\text{C}$ . Only isolated cases of recrystallization have been reported at this temperature, which is consistent with the recrystallization behavior reported in Moreno et al. and Xu et al. Transmission electron microscopy was used to observe the  $\gamma'$  precipitates, which showed different sizes and morphologies before and after the recrystallization. Carter investigated the applicability of the conventional solution heat treatment temperature at  $1230^\circ\text{C}$  for 2 h for L-PBF samples [9]. The results showed that the temperature of  $1260^\circ\text{C}$  for 2 h produced finer  $\gamma'$  precipitates than those produced at the conventional heat-treatment temperature of  $1230^\circ\text{C}$ . Thus, the former was more suitable for L-PBF. However,  $1260^\circ\text{C}$  is still less than the  $\gamma'$  dissolution temperatures of  $1269^\circ\text{C}$  and  $1288^\circ\text{C}$  obtained from the differential scanning calorimetry (DSC) measurements and ThermoCalc calculations, respectively. Thus, at  $1260^\circ\text{C}$  the  $\gamma'$  precipitates could not dissolve completely, as was evident from the conspicuous  $\gamma'$  precipitates in the micrographs. Carter explained that if the material was heated above  $1260^\circ\text{C}$ , there was a risk of melting because of the narrow temperature range between the  $\gamma'$  solvus and the incipient melting temperature. To close the defects observed in the as-built condition, hot isostatic pressing (HIP) was performed prior to the solution heat treatment. The slow cooling in the HIP furnace coarsened and overaged the  $\gamma'$  precipitates. Thus, solutioning ought to be done to refine the  $\gamma'$  grains prior to aging. The aging heat treatment was performed in two stages, and the  $\gamma'$  grains so produced were not very different in size and morphology from those obtained after the solution heat-treatment. Based on this, Carter recommended that a solution heat treatment without aging may be sufficient to obtain the desired  $\gamma'$  precipitates. Griffith et al. [3] investigated the microstructures of solution heat-treated ( $1260^\circ\text{C}$ ) Alloy 247LC and Hf-free Alloy 247LC. The microstructures of both the alloys showed large grains, which might have formed because of the recrystallization and growth. The grains in the Hf-free alloy were smaller and showed lower aspect ratio than those in the Alloy 247LC. The Hf-free alloy also showed annealing twins and fine  $\gamma'$  precipitates as compared to the Alloy 247LC. Nanoscale segregation was observed in the cells of Alloy 247LC in the as-built conditions, but the microstructure appeared to be homogenized after the heat treatment. The Alloy 247LC exhibited strain-age cracking, whereas the Alloy 247LC Hf-free resisted strain-age cracking after the HIP and solution heat treatments. After aging, the Hf-free alloy showed lower hardness than the Alloy 247LC. Engeli [5] investigated the effect of heat treatment on the recrystallization of samples printed with different process parameters. Because different process parameters can produce different amounts of plastic strain, and hence stored energy, their response to recrystallization could be different. Indeed, Engeli's results showed that different process parameters caused different degrees of recrystallization, which was evident from the differences in the grain sizes (linked to recrystallization and grain growth) of the heat-treated samples. In the

present paper, design of experiments (DOE) was used to investigate the effect of the process parameters on the grain size of solution heat-treated samples. The process parameters investigated in this study attained energy density ranges (high, medium, and low), which produces or resists solidification cracks during printing. This is different from Engeli's study, which investigated only the process parameters that were within the range that produced solidification cracks. Hence, the present study provides insight into the recrystallization behavior of Alloy 247LC and the transition of its microstructure from being solidification crack-susceptible to solidification crack-resistant. Understanding the behavior of the solidification crack-resistant heat-treated microstructure of an alloy is particularly important as the suppression of cracks improves the properties of the alloy. The formation of recrystallized grains of an optimum size can further improve the properties of the alloy. Furthermore, this paper investigated the influence of the as-built grain-size on the final heat-treated grain size which was not reported in Engeli. Finally, the solid-state cracking, phases, microconstituents, homogenization and microhardness of the heat-treated microstructure of the Alloy 247LC were revealed.

## 2. Experiment

In this study the feedstock metal powder Sandvik Osprey™ Alloy 247LC was produced using a vacuum induction melting furnace with subsequent gas atomization using argon gas. The powder was sized into a powder particle size distribution of 15–53  $\mu\text{m}$ . The composition of the Alloy 247LC powder used in this study is listed in Table 1. O and N content were below 200 ppm.

Thirty cubes (numbered 1 to 30) with the dimensions of 15 mm  $\times$  15 mm  $\times$  15 mm were printed in EOS M290 machine. The EOS M290 machine used in this study operated a maximum laser power of 400 J/s and a continuous-wave Yb fiber laser with a spot size of 70  $\mu\text{m}$ . It had an optical system with an F-theta lens and a high-speed scanner. The equipment used argon shielding gas to prevent oxidation. The stripe scanning strategy was utilized in the current process. This strategy rotated the laser scanning in a new layer by 67° relative to the previous layer. Details about this scanning strategy is given in Leicht et al. [24]. The following process parameters were varied to manufacture the cubes: the laser power (170–220 J/s), scanning speed (2800–3200 mm/s), and hatch distance (20–40  $\mu\text{m}$ ). A constant layer thickness of 20  $\mu\text{m}$  was applied. A full factorial DOE was performed using MODDE software to produce 27 combinations of the process parameters. The process parameter combination of the mid-point values of 195 J/s, 3000 mm/s, and 30  $\mu\text{m}$  (used in sample 14) was repeated three times (used in samples 28, 29 and 30). The DOE has been used in a previous study on the effect of the process parameters on the quantity of defects [6]. The results were analyzed in MODDE using the response surface method, which is also described in Ref. [6]. Six extra samples (31–36) were also manufactured with manually assigned process parameters. A cross-section measuring approximately 15 mm  $\times$  15 mm  $\times$  3 mm was cut from each cube. Thirty-six cross-sections of the process parameters (1–36) were solution heat-treated at 1260 °C for 2 h in a vacuum furnace with flowing argon gas. The heating rate was 5 °C/min. After the heat treatment, the samples were immediately quenched in water. Table 2 displays the sample identification numbers and the values of the L-PBF process parameters (laser power (power), scanning speed (speed) and hatch distance (hatch)) utilized to process the samples. The last column contains the volumetric energy density which is calculated according to

**Table 2**

Sample identification numbers and corresponding process parameters. The samples in the as-built condition were assigned numbers 1 to 36. The samples in the solution heat-treated condition were assigned 1HT to 36HT.

Sample number As-built (heat-treated)	Power (J/s)	Speed (mm/s)	Hatch ( $\mu\text{m}$ )	Energy density ( $\text{J}/\text{mm}^3$ ) <sup>a</sup>
1 (1HT)	170	2800	20	152
2 (2HT)	195	2800	20	174
3 (3HT)	220	2800	20	196
4 (4HT)	170	3000	20	142
5 (5HT)	195	3000	20	163
6 (6HT)	220	3000	20	183
7 (7HT)	170	3200	20	133
8 (8HT)	195	3200	20	152
9 (9HT)	220	3200	20	172
10 (10HT)	170	2800	30	101
11 (11HT)	195	2800	30	116
12 (12HT)	220	2800	30	131
13 (13HT)	170	3000	30	94
14 (14HT)	195	3000	30	108
15 (15HT)	220	3000	30	122
16 (16HT)	170	3200	30	89
17 (17HT)	195	3200	30	102
18 (18HT)	220	3200	30	115
19 (19HT)	170	2800	40	76
20 (20HT)	195	2800	40	87
21 (21HT)	220	2800	40	98
22 (22HT)	170	3000	40	71
23 (23HT)	195	3000	40	81
24 (24HT)	220	3000	40	92
25 (25HT)	170	3200	40	66
26 (26HT)	195	3200	40	76
27 (27HT)	220	3200	40	86
28 (28HT)	195	3000	30	108
29 (29HT)	195	3000	30	108
30 (30HT)	195	3000	30	108
31 (31HT)	195	3000	30	108
32 (32HT)	195	3000	30	108
33 (33HT)	180	2800	30	107
34 (34HT)	180	3000	30	100
35 (35HT)	210	2800	30	125
36 (36HT)	210	3000	30	117

<sup>a</sup> This is the volumetric energy density which includes the constant layer thickness of 20  $\mu\text{m}$ .

Eq. (2) that includes the layer thickness (layer).

$$\text{volumetric energy density} = \text{power}/(\text{speed} \times \text{hatch} \times \text{layer}) \quad (2)$$

The samples were mounted in a hot mounting resin, ground, and polished to a surface with mirror finish. They were then etched in the Kalling's reagent (4 g  $\text{CuCl}_2$ ; 80 mL HCl; 80 mL ethanol) for 10 s. The samples were preliminarily examined using a Zeiss Axio light optical microscope. Subsequently, the cracks and grains were examined using TM 3000 Hitachi scanning electron microscope (SEM). The grain width was measured by applying the linear intercept method to three micrographs taken randomly at 100 $\times$  magnification for each sample. A similar approach was used to measure the grain height. Samples 3, 30, and 22 were fabricated with the high, medium, and low energy densities, respectively (196, 108, and 71  $\text{J}/\text{mm}^3$ , respectively). The samples were examined under the as-built and heat-treated conditions using a Zeiss Gemini 450 field emission gun scanning electron microscope equipped with an electron backscattered diffraction (EBSD) detector from the Oxford Instruments Symmetry system. The samples were examined in both the secondary electron (SE) and backscattered electron (BSE)

**Table 1**

Chemical composition of the Sandvik Osprey™ Alloy 247LC VIGA powder (wt%).

C	Cr	Ni	Co	Mo	W	Ta	Ti	Al	B	Zr	Hf
0.07	8.5	Bal.	8.7	0.6	9.2	3.5	0.7	5.5	0.012	0.01	1.24
Si	Mn	S									
<0.01	<0.01	<0.003									

modes. EBSD data were processed and analyzed using the Aztec and Aztec crystal software packages from Oxford Instruments. For texture analysis, the inverse pole figures (IPFs) and PFs of the samples were obtained. To investigate possible recrystallization of the samples, their grain orientation spread (GOS) and geometric necessary dislocation (GND) density data and maps were generated using Aztec crystal software. Finally, the grain area and aspect ratio data were generated. For the generated data, a threshold angle of  $10^\circ$  was set in the Aztec crystal software to identify the grains. DSC measurements were carried out on a NETZSCH STA449C thermo-microbalance system. The measurements were conducted under an argon atmosphere with an argon flow rate of 50 mL/min. The DSC sample was first heated from room temperature ( $\approx 23^\circ\text{C}$ ) to  $600^\circ\text{C}$  at a heating rate of  $20^\circ\text{C}/\text{min}$ , and then the sample was held and stabilized at  $600^\circ\text{C}$  for 60 min. The sample was then heated from  $600$  to  $1400^\circ\text{C}$  at a heating rate of  $5$  or  $10^\circ\text{C}/\text{min}$ , and maintained at  $1400^\circ\text{C}$  for 10 min. The sample was then cooled from  $1400$  to  $600^\circ\text{C}$  at a cooling rate of  $5$  or  $10^\circ\text{C}/\text{min}$ . Each sample was subjected to two measurement cycles. The first and second measurement cycles were named first and second loop respectively. Samples 31 and 34 were analyzed under the as-built condition. Subsequently, the DSC measurement was also performed on sample 31 after the solution heat treatment (31HT). Microhardness measurements were performed on the samples 1HT–30HT using a Struers Duramin-40 Vickers microhardness tester. The indents were made for 10 s using a 0.5 kgf load (HV0.5). Nine indents were performed on the cross-section of each sample and were spread in the upper, middle, and lower regions of the cross-section. This corresponds to three indents located in the upper, three indents located in the middle and three indents located in the lower regions. Two indents were always spaced at approximately 5 mm from each other along the length and width of the sample cross-section.

### 3. Results

#### 3.1. Cracking

The initial optical microscopy examination revealed the presence of millimeter-length cracks, along the grain boundaries, in all the heat-treated samples. These millimeter-length solid-state cracks were much larger than the micrometer-length solidification cracks previously reported in the as-built samples [6]. This indicates that the heat treatment resulted in the generation of solid-state cracks in the samples. Though sample 30 was reported to resist solidification cracking in the as-built condition, it revealed the millimeter-length solid-state cracks after the

solution heat-treatment. Fig. 1a shows examples of the solid-state cracks in sample 22 under the heat treatment condition (referred to as 22HT). An example of the solidification cracks observed in the corresponding as-built sample 22 is indicated with the red arrow in Fig. 1b.

#### 3.2. Influence of the L-PBF process parameters on the heat-treated grains

To investigate the heat-treated microstructure of the samples, it was compared with their as-built microstructure. A preliminary optical microscope examination revealed that the grain sizes of the samples varied. Samples 3, 30, and 22 were subsequently observed using SEM. Fig. 2 shows the SEM images of the grains in samples 3, 30, and 22 under the as-built condition.

The microstructure was characterized by elongated columnar grains that grew in the build direction. This was similar to the observations in Wang et al. [10] and Divya et al. [11]. These columnar grains solidified epitaxially on a previously formed layer. The grain size of the as-built samples was small. The grains of sample 3 were larger than those of sample 30. Sample 22 displayed the smallest grain size. The average grain areas in samples 3, 30 and 22 were  $423$ ,  $250$  and  $100\ \mu\text{m}^2$  respectively. The grain sizes were clearer in the IPFs and charts presented later. At higher magnifications, subgrains could be observed in all the samples (Fig. 3a). The subgrains consisted of cells and numerous bright spherical particles and microconstituents, as shown in Fig. 3b and c, where the red arrows indicate the spherical particles between the cells. Less bright microconstituents (typically  $\gamma/\gamma'$ ) were also present between the cells, as indicated by the blue arrows. The as-built microstructure of the alloy was similar to that reported in Ref. [10,11,22]. The cells were reported to have low misorientation angle and high dislocation density.

The cell diameters in samples 3, 30 and 22 were between the range of  $0.3$  and  $1\ \mu\text{m}$ . Even within each sample, cell diameters differed considerably which demonstrated that there were local variations in the cooling rates. In Fig. 3b, the diameter of clearly identifiable cells was between approximately  $0.4$  to  $0.7\ \mu\text{m}$ . The bright spherical particles were previously identified by X-ray diffraction to be MC carbide [11]. X-ray elemental mapping also indicated that the particles contained C together with the MC carbide formers: Hf, Ta, W and Ti. However, some particles were reported to contain O suggesting that they were oxides [10,11]. In Fig. 3b, the bright spherical particles indicated with the red arrows were between the range of approximately  $0.1$  and  $0.13\ \mu\text{m}$  diameter. Fig. 3c displayed a bright spherical particle (indicated with the red arrow) of approximate  $45\ \text{nm}$  diameter. Much smaller bright particles, with diameters estimated to be below  $10\ \text{nm}$ , could be observed in the micrograph. The tip of the  $\gamma/\gamma'$  previously displayed in Fig. 3b could be observed in Fig. 3c (indicated with the blue arrow).

After the heat treatment, the grain size of all the samples increased. The grains in samples 3HT and 30HT were larger than those in sample 22HT. Fig. 4 shows the grains in samples 3HT, 30HT, and 22HT. The increase in the grain size can be observed by comparing Figs. 2 and 4. The average grain area of sample 3HT, 30HT and 22HT were  $2654$ ,  $3366$  and  $1534\ \mu\text{m}^2$  respectively.

At higher magnifications, the cell structure observed under the as-built condition shown in Fig. 3 was no longer visible under the heat-treatment condition. The higher-magnification HT microstructure is shown in Fig. 5. Twinning could be observed as indicated by the red arrows in Fig. 5a and b. This suggested that recrystallization occurred. The bright spherical particles were still present which was clearly visible in Fig. 5c.

Fig. 5d displayed an image of a bright particle. Here, in Fig. 5d, the diameter was approximately  $0.2\ \mu\text{m}$  which was bigger than the largest bright particle previously observed in Fig. 3b (the samples in Fig. 3b and 5d were 30 and 30HT respectively). In addition, no small bright particles were observed close to the big particle in Fig. 5d. Recall that small particles of different sizes were observed in Fig. 3c. Note that the areas of the two micrographs are approximately equal and can be measured from

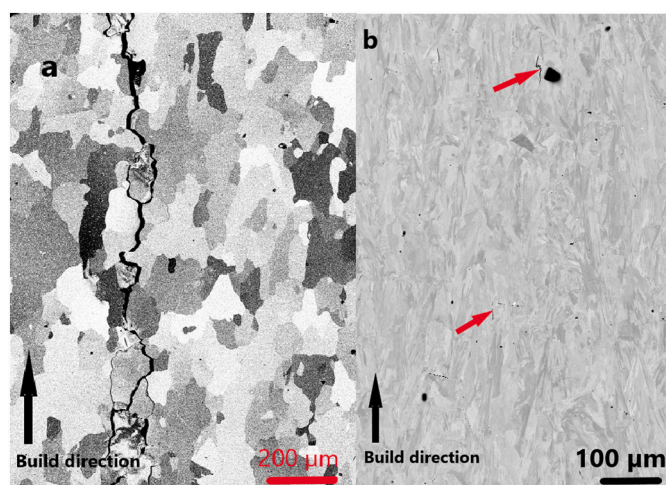
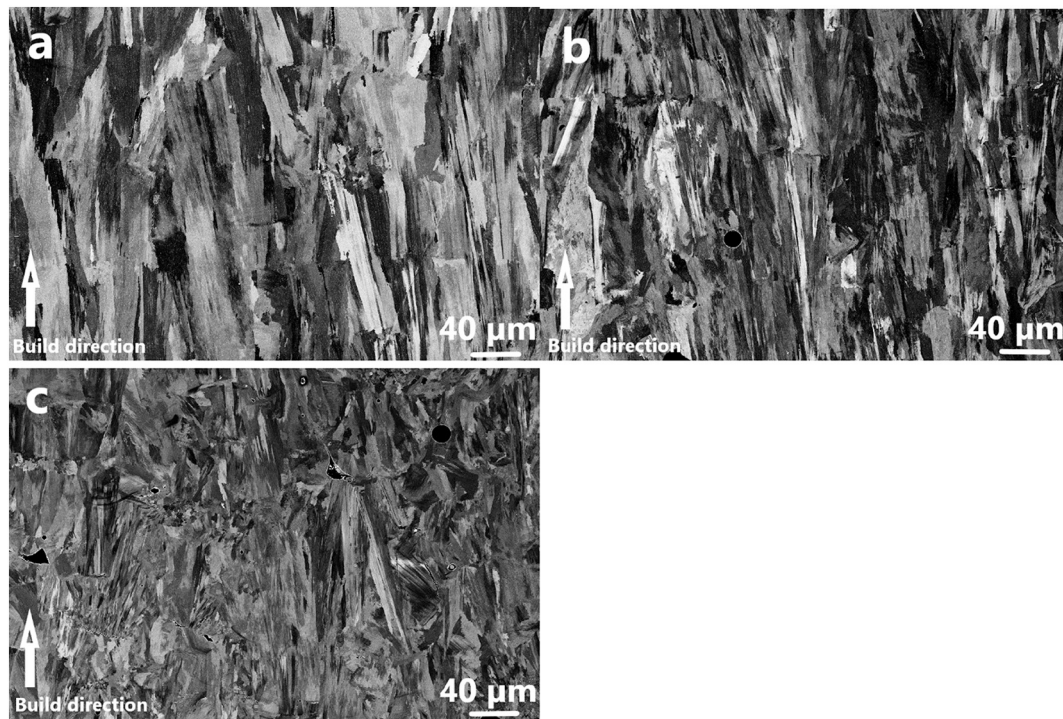
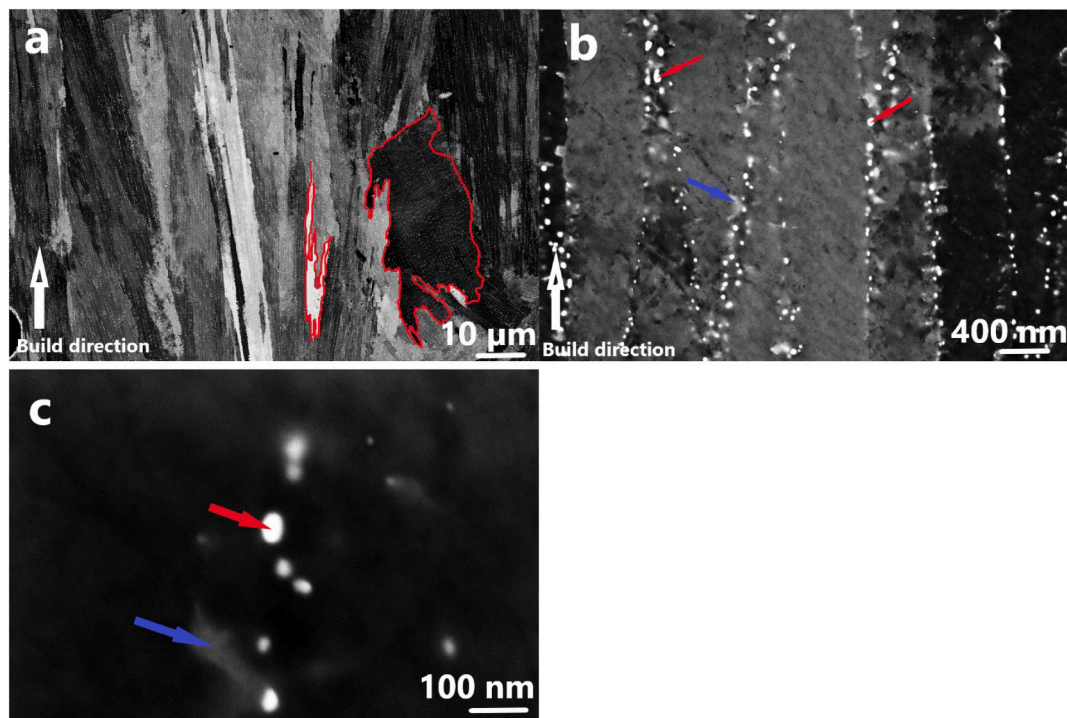


Fig. 1. (a) Solid-state cracking at the grain boundaries of 22HT (b) Solidification cracks (indicated by red arrow) in 22. (For interpretation of the references to colour in this figure legend, the reader is referred to the web version of this article.)



**Fig. 2.** SEM images of the grains in the as-built condition: (a) sample 3 showed the largest grains, (b) sample 30 showed large grains, and (c) sample 22 showed the smallest grains.



**Fig. 3.** (a) Approximate boundaries of the subgrains are marked in red. Cells were visible inside the dark subgrains. (b) Cell containing the bright spherical particles and microconstituents in the boundaries (examples of the bright spherical particles are marked with the red arrows and a less bright microconstituents are marked with the blue arrow). (c) Higher magnification image of bright spherical particles (an example is indicated with the red arrow) and less bright  $\gamma/\gamma'$  (indicated with the blue arrow). (For interpretation of the references to colour in this figure legend, the reader is referred to the web version of this article.)

the similarly sized scale bars. Thus, it appears that the particle in Fig. 5d coarsened at the expense of smaller particles that were previously located close to it. This is in line with the phenomenon of Ostwald ripening. Similar observations were made for other micrographs which

suggested that the particles coarsened after heat-treatment. Therefore, it was suspected that the average size of the bright particles found in the as-built condition increased under the heat-treatment condition. However, to obtain a statistically valid result, it is necessary to quantify the

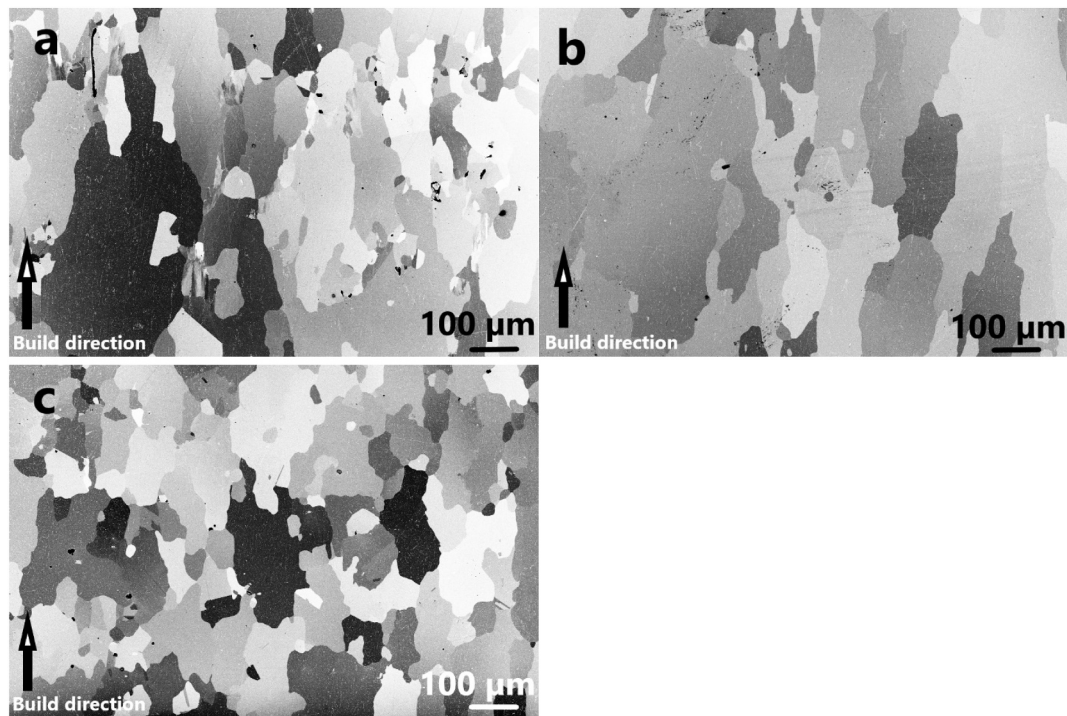


Fig. 4. Heat-treated grain structure with bigger grains than those observed in the as-built condition. (a) 3HT (b) 30HT (c) 22HT.

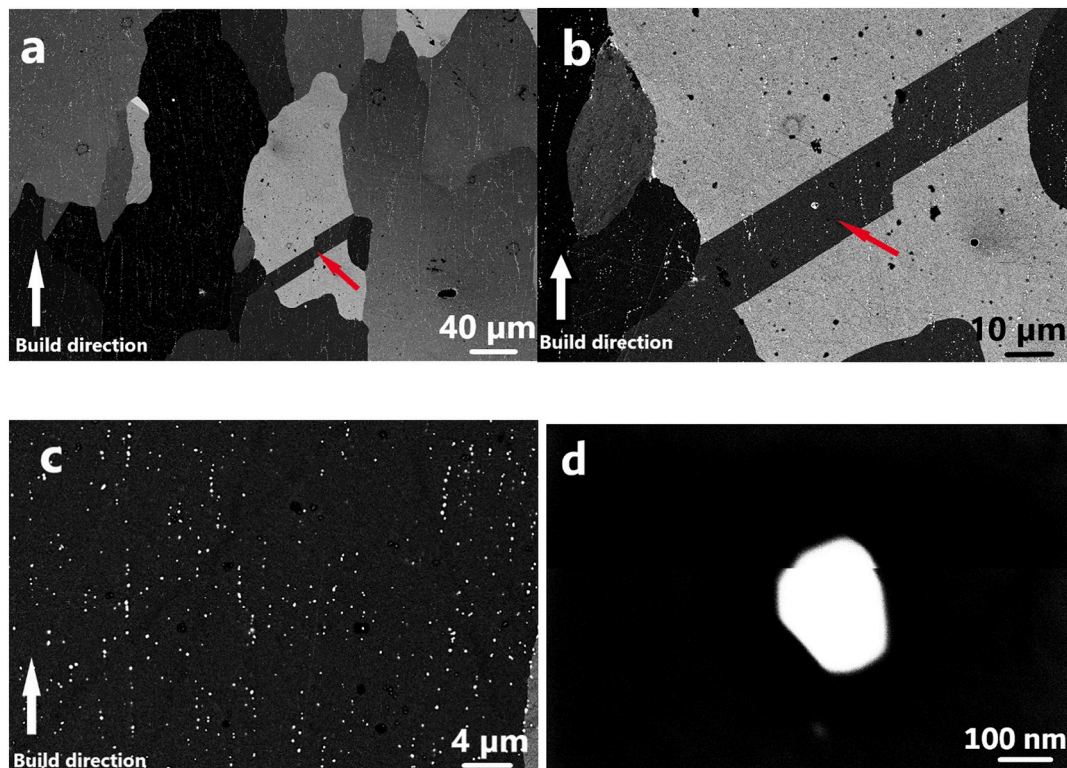


Fig. 5. Heat-treated grain displaying: (a) bright particles and twinning (twinning indicated by the red arrow), (b) bright particles and twinning at higher magnification, (c) distinct bright particles, followed the build direction and (d) a bright particle. (For interpretation of the references to colour in this figure legend, the reader is referred to the web version of this article.)

average size of the particles over a large area of the sample as the sizes of the particles may vary locally because of the difference in the cooling rate. The average size of the particles was not quantified in the present study. It was previously stated that these bright particles are MC

carbides under the as-built condition. Divya et al. [11] suggested that the MC carbide in the as-built condition were retained and were more stable after solution heat-treatment at 1230 °C. It is known, from cast superalloys, that MC carbide formed during solidification [1]. It is also

known that the MC carbides could degenerate into  $M_{23}C_6$  or  $M_6C$  carbides during subsequent heat-treatments [1,25]. However, these carbide transformations occurred at a lower temperature (commonly between 790 °C to 816 °C and 816 to 982 °C for  $M_{23}C_6$  and  $M_6C$  respectively) than the 1260 °C in which the present samples were heat-treated which was followed by quenching. Thus, it was not likely that  $M_{23}C_6$  and  $M_6C$  carbides were present and most likely that the MC carbides formed during L-PBF processing were retained under the solution heat-treatment condition. It is to be noted that the X-ray elemental mapping performed by Divya et al. [11] and Wang et al. [10] showed that the particles contained Hf and Ta; these elements form very stable MC carbides [1,25]. According to the DSC results presented in Section 3.4,

the carbide dissolution temperatures in the samples were  $\geq 1350$  °C (these were the carbide transformation temperatures observed in both the as-built and heat-treated conditions) which matched the dissolution temperature of MC carbide. Thus, the bright precipitates present in the microstructure in Fig. 5 are most likely MC carbides. However, more advanced characterization is required to determine the crystal structure and lattice parameters to properly identify the MC carbide and describe how it evolved under the L-PBF and solution heat-treatment conditions.

The grain size, aspect ratio and texture of samples 3, 30, and 22 were examined in detail by generating their IPFs from the EBSD data. Fig. 6 shows the IPFs of samples 3, 30, and 22 in both the as-built and heat-treated conditions.

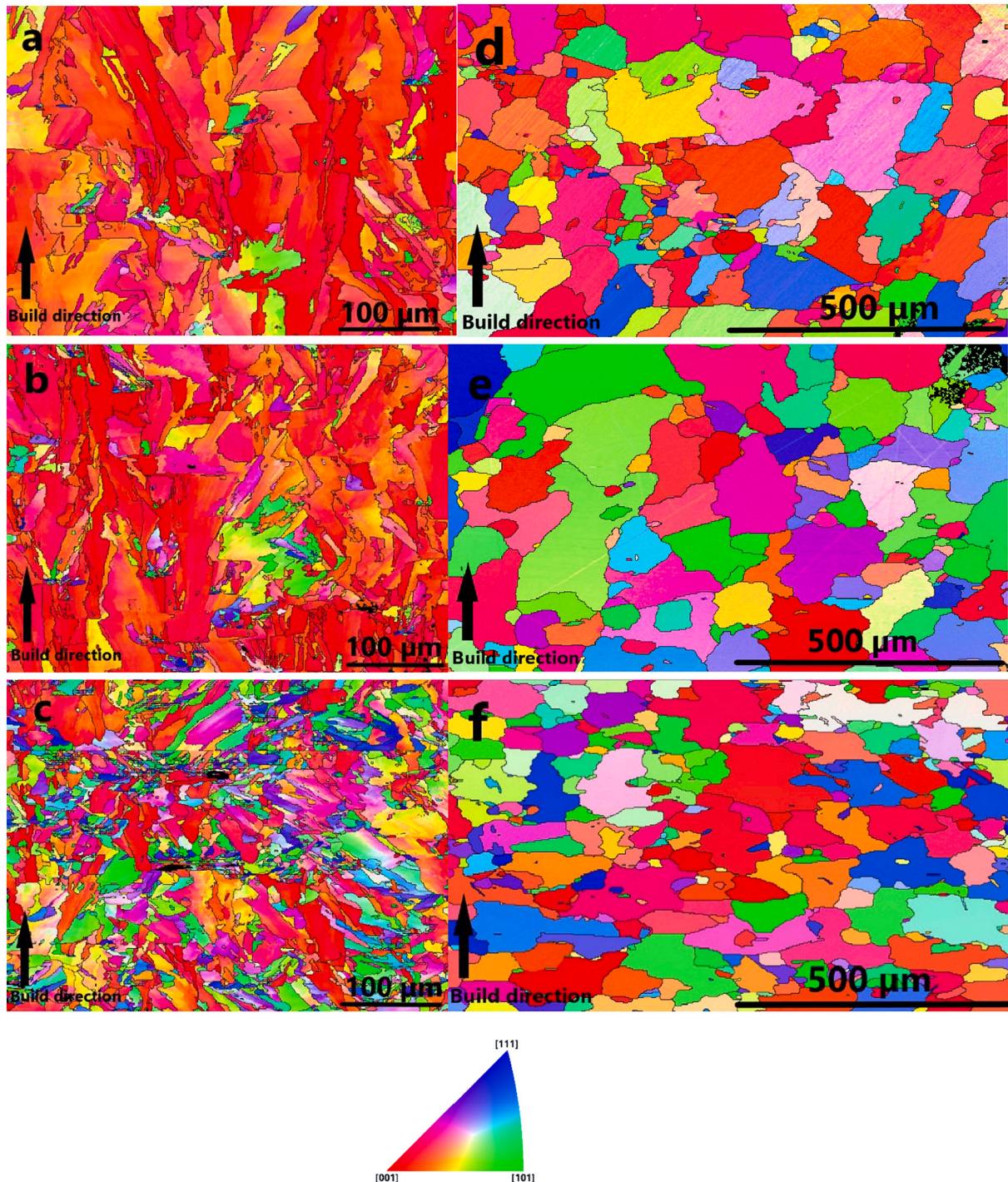


Fig. 6. IPFs (produced parallel to the build direction) of the grains under the as-built and heat-treated conditions. (a) 3 (b) 30 (c) 22 (d) 3HT (e) 30HT (f) 22HT.

The IPFs also indicated that the grains in the heat-treated samples were larger than those in the as-built samples. The as-built texture observed in samples 3 and 30 had a strong  $\langle 001 \rangle$  direction, whereas sample 22 showed weak as-built texture. Several elongated grains in samples 3 and 30 in Fig. 6a and b extended beyond  $100\ \mu\text{m}$  which means that they extended across several layers in the build direction. Recall that each powder layer was  $20\ \mu\text{m}$  thick. It was also observed that these relatively large grains produced the strong  $\langle 001 \rangle$  direction (evidenced by their red colour). In contrast, several of the smaller grains did not orientate in the  $\langle 001 \rangle$  direction (for example the green- and yellow-colored grains in Fig. 6a and b). Thus, the red grains clearly demonstrated the largest average size. It was likely that the grains of samples 3 and 30, which were favorably aligned in the  $\langle 001 \rangle$  direction, parallel to the direction of heat flow, solidified epitaxially and grew competitively at the expense of less favorably aligned grains. These favorably aligned red grains could increase their sizes, as they grew, while also maintaining the  $\langle 001 \rangle$  direction. In contrast, the green grains which had the  $\langle 101 \rangle$  direction, got outgrown during the competitive growth and thus remained small. However, the grain evolution was rather complicated to describe and this was due to the complex melting, solidification, heating and cooling patterns typical of the L-PBF process. The texture after the heat treatment had a weak texture. The texture of the samples under different conditions can also be observed from the PFs shown in Fig. 7.

A strong texture in the  $\langle 001 \rangle$  direction was observed in samples 3 and 30; however, this texture reduced in sample 22, which showed diffuse clusters with the lowest multiples of uniform densities (MUD) value of 2.82. This is consistent with the reduced texture observed in the IPF plot of 22 (Fig. 6). Samples 3HT, 30HT and 22HT showed smaller clusters at more varied locations than samples 3, 30 and 22. This indicates that the  $\langle 001 \rangle$  crystals did not align in a particular sample direction, that is, a low texture. This is consistent with the IPF results.

Three IPFs and PFs (similar to those shown in Figs. 6 and 7) were generated at random locations in each sample. Figs. 6 and 7 are representative of the results of the other plots. Fig. 8 shows the average grain area and aspect ratios of these three samples.

The analysis carried out in MODDE modeled the responses of the grain width, grain height, and aspect ratio of the 30 samples to the power, speed, and hatch. The methodology used is described in a previous study [6]. The software calculated the process parameters that significantly influenced the grain width, grain height, and aspect ratio of the samples. The as-calculated  $P$ -values are listed in Table 3. When the  $P$  value was  $<0.05$ , the above-mentioned factors significantly affected the response of the measurements (grain width, height and aspect ratio) to them. The  $P$  values were also calculated for the combination of two factors. For example, power\*hatch refers to the effect of both the power and hatch on the response.

As can be observed from Table 3, the laser power significantly influenced the height, width, and aspect ratio. The scanning speed significantly influenced the height and aspect ratio. In addition, the most significant process parameters influencing the height, width, and aspect ratio of the samples were the laser power, laser power\*hatch distance, and laser power, respectively, as indicated by the lowest  $P$  values in each column. The significance of the process parameters can be visualized by observing the charts in Fig. 9, which show the effect of laser power, scanning speed, and hatch distance on the height and width of the grains.

The grain height increased with an increase in the laser power from 170 to 220 J/s. MODDE calculated this trend to be significant, as evidenced by the low  $P$  value of  $1.466\text{e-}06$  (Table 3). The effect of the scanning speed on the grain width did not show any trend, which also corresponds to the non-significant high  $P$  value of 0.640. The other charts can be interpreted in a similar manner.

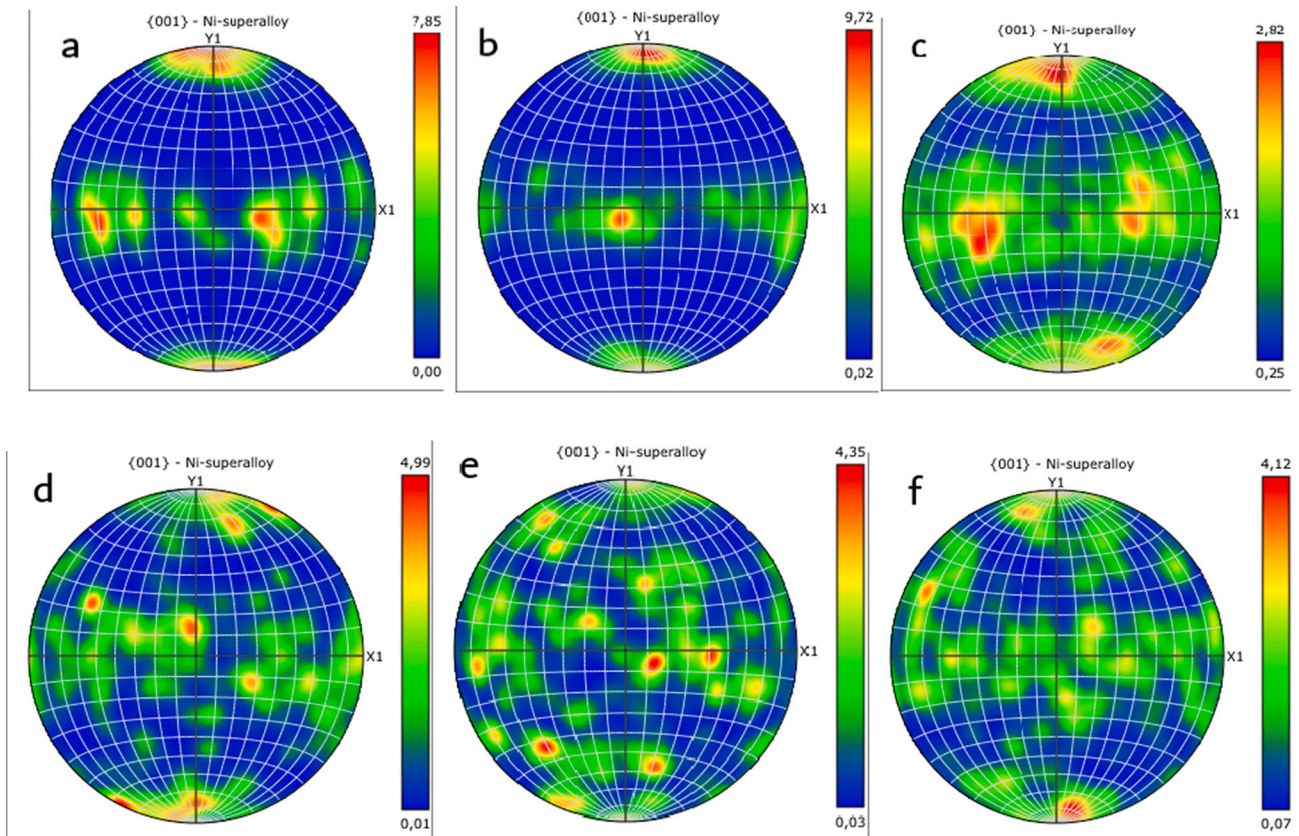


Fig. 7. PFs of  $\langle 001 \rangle$  under the as-built and heat-treated conditions. (a) 3 (b) 30 (c) 22 (d) 3HT (e) 30HT (f) 22HT.

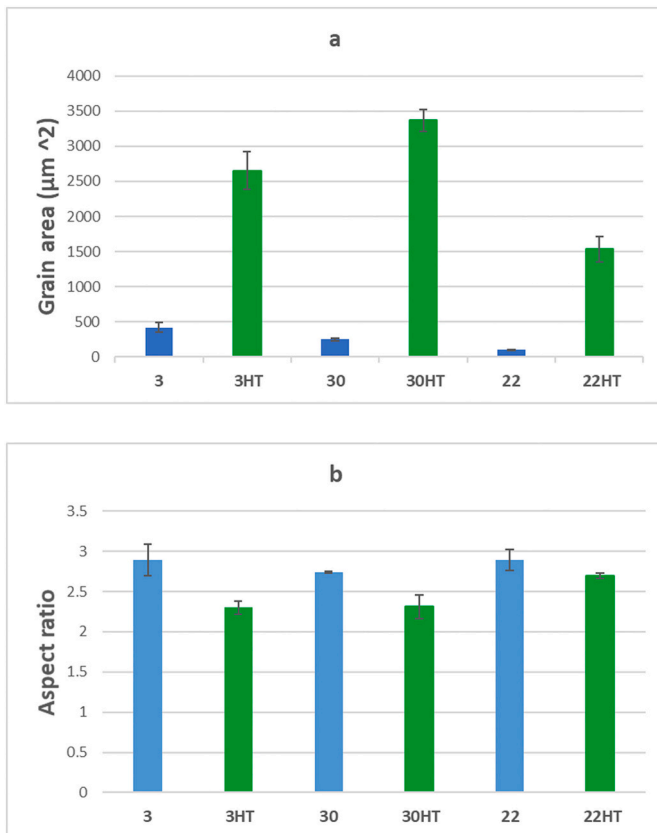


Fig. 8. (a) Average grain areas of the samples under the as-built and heat-treated conditions. (b) Average aspect ratios of the samples under the as-built and heat-treated conditions.

Table 3

P values calculated using MODDE for the factors (laser power, scanning speed, and hatch distance) that had significant (significant values are marked in bold) and non-significant influence on the responses (grain height, width, and aspect ratio of the grains).

Factors	P value of the height	P value of the width	P value of the aspect ratio
Power	<b>1.466e-06</b>	<b>0.002</b>	<b>7.096e-18</b>
Speed	<b>0.003</b>	0.640	<b>0</b>
Hatch	0.100	<b>0.049</b>	0.436
Power*Hatch	<b>0.040</b>	<b>0.001</b>	0.901
Power*Speed	0.953	0.689	0.664
Speed*Hatch	0.449	0.121	<b>0.041</b>

### 3.3. Recrystallization

To confirm that recrystallization occurred, GOS data and maps were generated. GOS measures the average orientation of a grain relative to the average local orientation of the points in the grain [5,26]. Thus, every grain possesses a specific GOS value. The GOS values of samples 3HT, 30HT, and 22HT were lower than those of samples 3, 30, and 22 respectively. Fig. 10 shows the GOS values of samples 22 and 22HT.

In Fig. 10a, the red grain in sample 22 has a GOS value of  $7.88^\circ$  suggesting that it was severely plastically strained. The blue colour in Fig. 10b (which indicates a low GOS value close to zero) is spread over a large fraction of sample 22HT, indicating that most of the grains were recrystallized. However, the red grains in Fig. 10b have a GOS value of  $4.19^\circ$  indicating that they were not recrystallized. The orange grain has GOS values of  $3.7^\circ$  also indicating that it was not recrystallized. To further clarify the extent to which recrystallization occurred, it was

necessary to measure the fraction of the recrystallized grains. This measurement was performed by first defining the GOS value of a recrystallized grain. Ayad et al. [27] stated that a grain with a  $\text{GOS} \leq 2^\circ$  is recrystallized. Xu [23] used a more moderate value of  $\text{GOS} < 1^\circ$  to identify the grains recrystallized after the heat treatment of an L-PBF-printed Alloy 247LC. In this study, a  $\text{GOS} < 1^\circ$  was used and grains with  $\text{GOS} < 1^\circ$  were counted. The results showed that the fraction of grains of samples 3HT, 30HT, and 22HT with GOS values  $< 1^\circ$  were 0.58, 0.94, and 0.98, respectively. These values suggest that the samples showed a high degree of recrystallization. Similar to the GOS, the low GND densities of 3HT, 30HT, and 22HT as compared to those of samples 3, 30, and 22 indicated that recrystallization occurred in these samples after the heat treatment. It is known that the GND data correlate with the amount of plastic strain [27,28] and as such, a reduction in the plastic strain and hence stored energy is the driving force for recrystallization. The GND map is shown in Fig. 11. The relatively low GND density values (in blue) were spread over approximately the entire area in 22HT, whereas higher GND densities (in green) were spread over sample 22.

The average GND density of 22HT was  $0.08 \times 10^{14}/\text{m}^2$ , whereas that of 22 was  $1.56 \times 10^{14}/\text{m}^2$ . Here, the former is approximately twenty times lower than the latter. Fig. 12 shows the average GND densities in three similar micrographs for each sample.

### 3.4. $\gamma'$ precipitate and microhardness

The  $\gamma'$  precipitate and bright spherical particles were observed in the samples after the heat treatment. A visual observation of samples 1HT-30HT showed that the  $\gamma'$  precipitate was still present in varying amounts in the samples. An example is shown in Fig. 13, where  $\gamma'$  is clearly visible.

Here, the area fraction of the  $\gamma'$  precipitate was 0.1, while that of the bright particles was 0.018. The diameter of the  $\gamma'$  precipitate discernible in the SEM image was approximately 80–300 nm. It is speculated that a smaller diameter  $\gamma'$  precipitate existed and could be discerned using high-resolution microscopy (for example, TEM). The composition of the Alloy 247LC in Table 1 was input to JMatPro, and the  $\gamma'$  precipitate transformation temperatures were modeled. The results are shown in Fig. 14. This shows that fully precipitated  $\gamma'$  showed a volume fraction of approximately 0.60. This precipitate completely dissolved at approximately  $1250^\circ\text{C}$ .

DSC experiments using a heating rate of  $5^\circ\text{C}/\text{min}$  were performed on sample 31, which was manufactured using the same process parameters as those used for sample 30. The heating diagram of the first loop revealed that the dissolution of the  $\gamma'$  precipitate occurred at approximately  $1250^\circ\text{C}$ , which is similar to the temperature calculated using JMatPro. Fig. 15 shows the first and second heating and cooling DSC curves of the samples. Thus, although the first loop heating curve (Fig. 15a) indicated that the dissolution of the  $\gamma'$  precipitate occurred at approximately  $1250^\circ\text{C}$ , the  $\gamma'$  precipitate could be observed even after heating to  $1260^\circ\text{C}$ . From the second loop heating curve (Fig. 15b),  $\gamma'$  dissolution could not be observed. In addition, the solidus was not distinct which is consistent with the DSC results reported previously [9,11]. In addition, the end of the heating curve shifted more to the right as the liquidus line moved from approximately  $1380^\circ\text{C}$  in the first loop to approximately  $1393^\circ\text{C}$  in the second loop heating. DSC measurement was also performed on 31HT. The transformation temperatures were similar to those reported for sample 31. These results are discussed later in Section 4.3.

The DSC experiment was repeated on sample 31, but at a higher heating rate of  $10^\circ\text{C}/\text{min}$ . Finally, DSC experiments were performed on sample 34 at the heating and cooling rates of 5 and  $10^\circ\text{C}/\text{min}$ . The  $\gamma'$ , carbide, and liquidus heating temperatures of all the samples are listed in Tables 4a and 4b.

The heat-treated samples showed relatively high microhardness values, confirming the existence of the  $\gamma'$  precipitate. To investigate the effect of the process parameters on the microhardness of the samples,

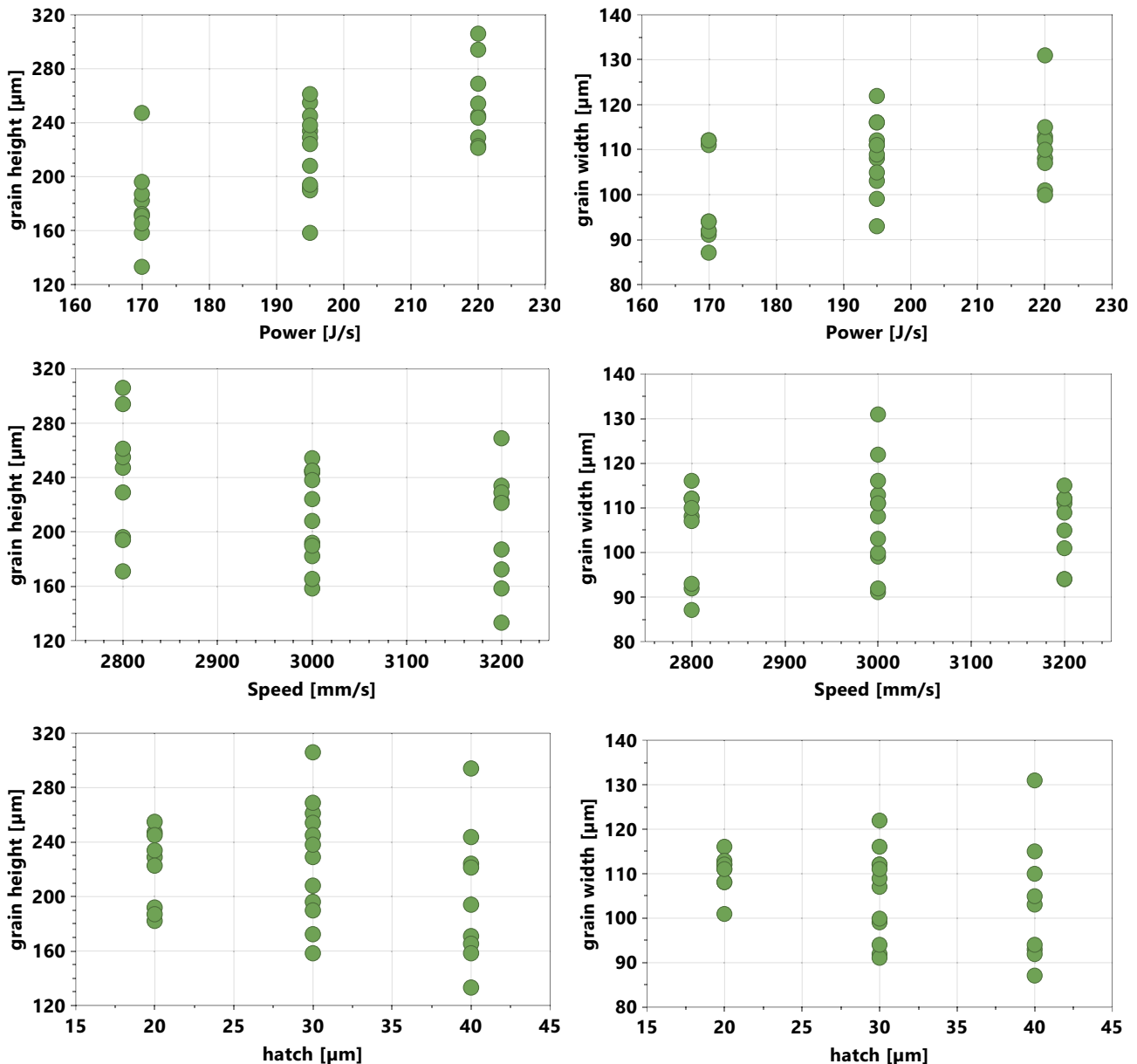


Fig. 9. Effects of the laser power, scanning speed, and hatch distance on the height and width of the grains. Green plots represent samples 1HT-30HT. (For interpretation of the references to colour in this figure legend, the reader is referred to the web version of this article.)

the microhardness values of samples 1HT-30HT were analyzed using MODDE. The results are shown in Fig. 16.

The microhardness plots were analyzed in a similar manner as described for Fig. 9, and the  $P$  values for the laser power, scanning speed, and hatch distance were calculated to be 0.16, 0.02, and 0.38, respectively. The  $P$  value for the scanning speed was slightly  $<0.05$ , indicating that it was significant. The  $P$  values of the laser power and hatch distance were  $>0.05$  thus they were not significant. This is contrary to the microhardness measurement results of as-built samples reported previously [6]. The laser power ( $P = 1.46588 \times 10^{-5}$ ) was strongly correlated with the microhardness. The scanning speed was not significant, while the hatch distance was slightly significant ( $P = 0.066$  and  $0.04$ , respectively). The microhardness of the HT samples was close to or higher than that of the as-built samples (Fig. 17).

## 4. Discussion

### 4.1. Cracking

A prominent feature of the heat-treated microstructure is the appearance of macrocracks. This is detrimental to the mechanical properties of the sample, even if all the other aspects of the microstructure are good. It has been reported that solid-state cracking occurs during the heat treatment of nickel-based superalloys. According to Boswell et al. [21], these cracks are either ductility dip or strain-age cracks. Strain-age cracking is also observed during the HIP of In 738LC [29]. Strain-age cracking was rationalized in the present study. It is well-known that alloys with high Al + Ti content ( $>4.5$  wt% according to Ref. [1]) are susceptible to strain-age cracking. Such alloys show a high  $\gamma'$  content, which precipitates rapidly. This causes localized strain in the grain boundaries, which promotes cracks when the stress is simultaneously being relieved. The Alloy 247LC with an Al + Ti content

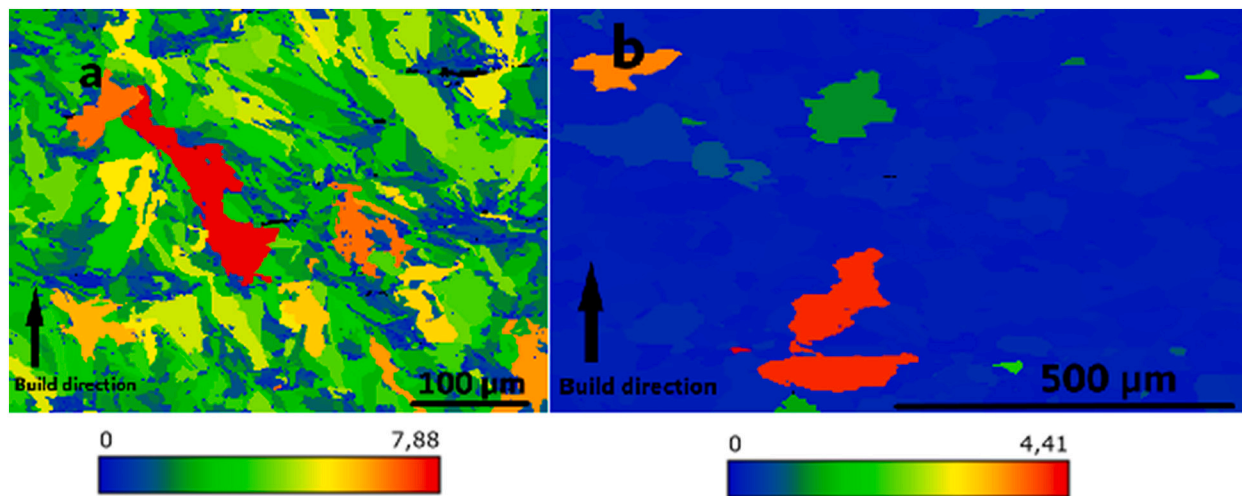


**Fig. 10.** GOS values of (a) 22 and (b) 22HT. The GOS value was low in most of the grains after the heat-treatment, whereas the GOS was higher in the as-built condition. The values in the heat map below the figures are in degrees.

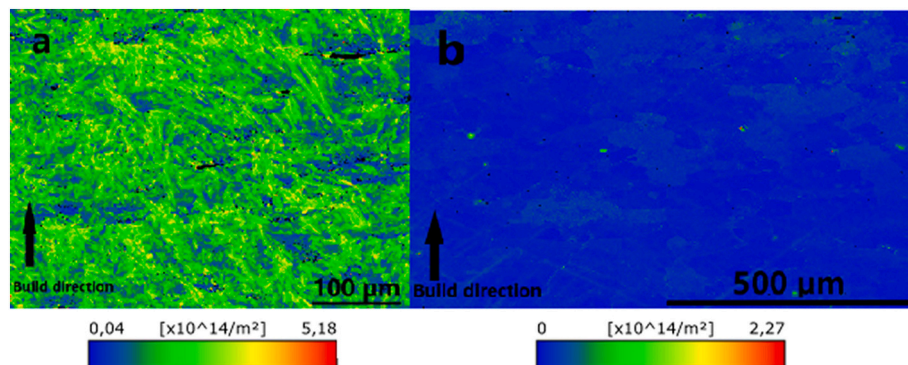


**Fig. 11.** GND density maps for (a) 22 and (b) 22HT. Sample 22HT showed lower GND density than sample 22.

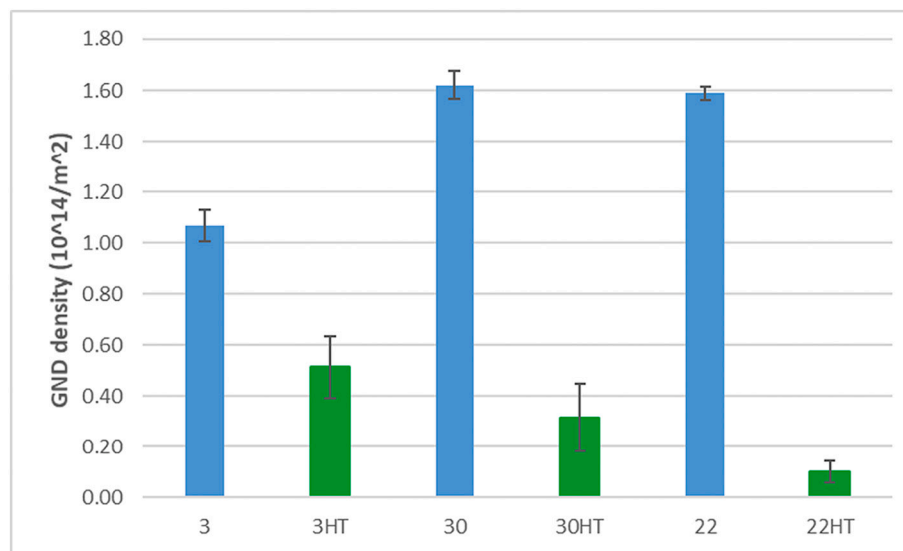


**Fig. 12.** GND density chart showing the reduction in the average GND density of the samples after the heat treatment.

of 6.2 wt% is susceptible to strain-age cracking. The volume fraction of  $\gamma'$  when fully precipitated was approximately 60%, which can also be observed from Fig. 14. The  $\gamma'$  precipitate time temperature transformation diagram (TTT) (15% volume fraction) as modeled in JMatPro

is shown as the green curve along with the heating rate plot in Fig. 18.

The green curve shows that the fastest  $\gamma'$  precipitation occurred in 4.41 s at 1120 °C. To avoid the  $\gamma'$  precipitation, rapid heating is recommended so as to avoid intersecting the TTT curve [30]. According to

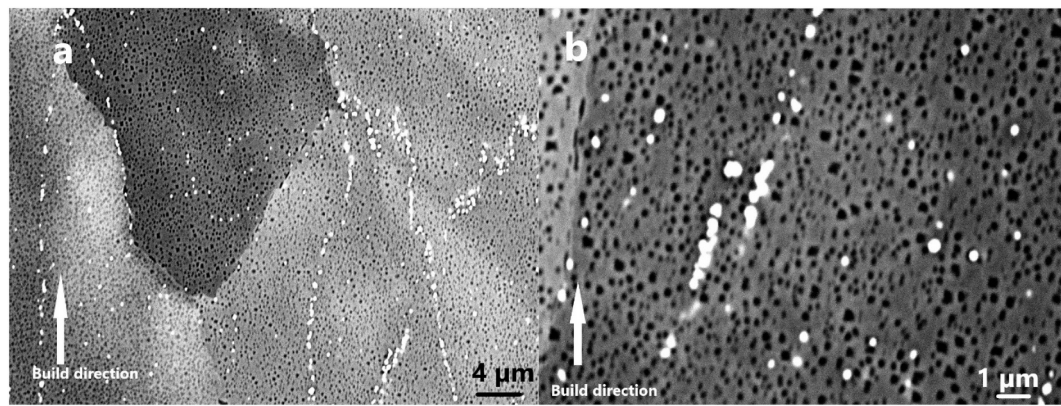


**Fig. 13.** (a)  $\gamma'$  precipitate and bright spherical particles in sample 2HT. (b) Higher magnification showing the  $\gamma'$  precipitate and bright spherical particles.

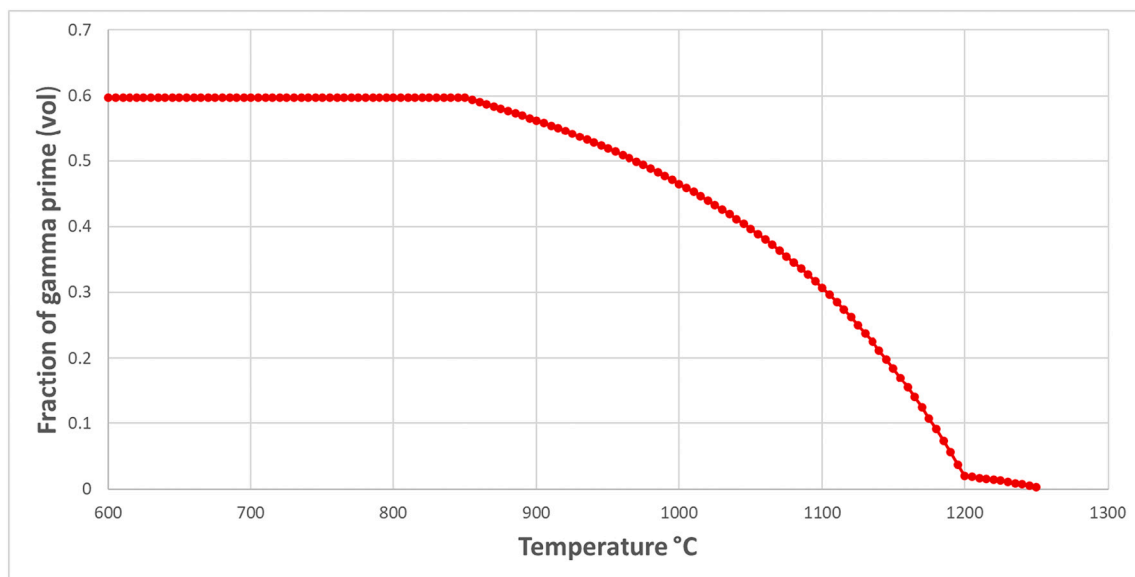


**Fig. 14.** JMatPro modeling of  $\gamma'$  precipitation in the Alloy 247LC.  $\gamma'$  precipitate volume fraction was approximately 0.60, and it dissolved at approximately 1250 °C.

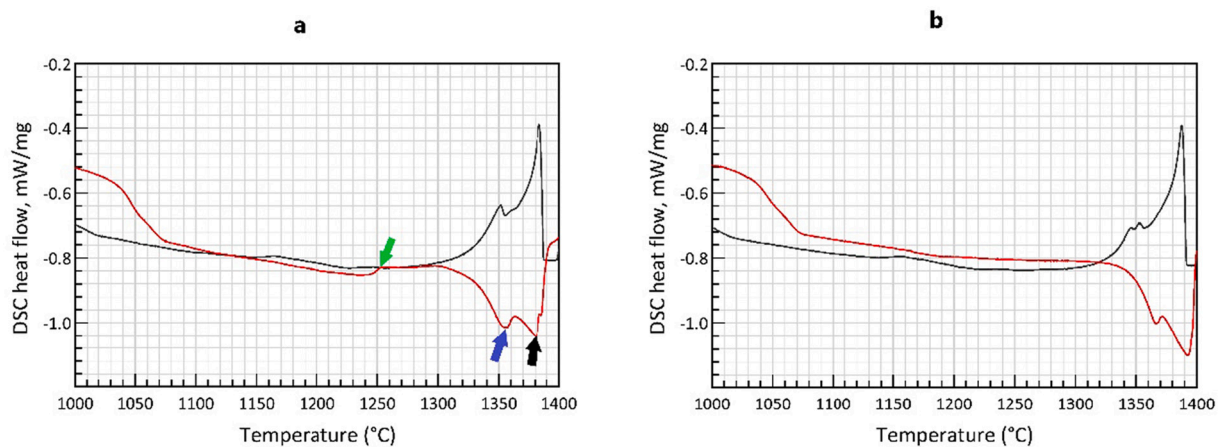


**Fig. 15.** DSC curves of heating (red) and cooling (black) performed on sample 31 (first loop) and then repeated on the same sample (second loop). (a) First loop  $\gamma'$  dissolution, carbide dissolution, and liquidus are marked with green, blue, and black arrows, respectively. (b) Second loop curves. (For interpretation of the references to colour in this figure legend, the reader is referred to the web version of this article.)

**Table 4a**

First loop DSC transformation temperatures.

Sample (heating rate)	$\gamma'$	Carbide	Liquidus
31 (5 °C/min)	1250 °C	1355 °C	1380 °C
31 (10 °C/min)	1250 °C	1357 °C	1382 °C
34 (5 °C/min)	1250 °C	1350 °C	1378 °C
34 (10 °C/min)	1250 °C	1355 °C	1380 °C

**Table 4b**

Second loop DSC transformation temperatures.

Sample (heating rate)	$\gamma'$	Carbide	Liquidus
31 (5 °C/min)	Not detected	1365 °C	1393 °C
31 (10 °C/min)	Not detected	1368 °C	1395 °C
34 (5 °C/min)	Not detected	1362 °C	1390 °C
34 (10 °C/min)	Not detected	1365 °C	1388 °C

Boswell et al., strain-age cracking begins above 750 °C. The blue curve indicates that to prevent cracking, the rapid heating of the samples from 750 to 1260 °C requires a heating rate of approximately 85 °C/s. However, if cracking occurs during the precipitation of a low volume fraction of the  $\gamma'$  precipitate (<15%), higher heating rates are required. This is because the green curve shifted to the left at a lower volume fraction of the  $\gamma'$  precipitate. The heating rate of 5 °C/min used in this study was too low to avoid the TTT curve and resist the strain-age cracking.

#### 4.2. Influence of the L-PBF process parameters on the heat-treated grains

Section 3.2 discussed the effects of the L-PBF process parameters on the grain size of the samples. Among all the process parameters investigated, the laser power affected the grain size most significantly. This

indicates that by adjusting the process parameters, mainly the laser power, the grain size of the heat-treated samples could be controlled. A useful observation here is that sample 30HT, which showed low crack density in the as-built condition (sample 30), exhibited a relatively large grain size as compared to samples 3HT and 22HT, as shown in Fig. 8a. The larger grain size in sample 30HT is therefore preferable for good creep resistance. However, the grain sizes of the samples were less than the range classified as fine grains (equiaxed grains of width 360  $\mu\text{m}$ ) for cast + heat-treated (solutioning and aging) Alloy 247 [31]. Therefore, sample 30HT may demonstrate lower creep resistance than its cast equivalent. The effect of the process parameters on grain size of the heat-treated samples has been investigated by Engeli [5]. In contrast to the present study, Engeli demonstrated that the scanning speed and hatch distance are the most significant process parameters affecting the grain size. The reason for this discrepancy may be due to the different values of the process parameters investigated in these two studies. Engeli explained that the plastic strain and stored energy characteristics at various L-PBF process parameters are the driving forces for the recrystallization of the grains of a sample subjected to heat treatment. This affects the recrystallization temperature or/and the grain-size of the heat-treated sample. The study explained that samples with higher plastic strain have higher nucleation rates, and hence produce smaller grain sizes. However, Engeli did not discuss the as-built microstructure, which could further influence the grain size. In the present study, the effects of the as-built microstructure of samples 3, 30, and 22 (printed with high, medium, and low energy density, respectively) on the grain size of the heat-treated samples 3HT, 30HT and 22HT were investigated.

Fig. 8a indicates that sample 22 showed the smallest grain size in the as-built and heat-treated conditions. Thus, it is ambiguous to relate the recrystallization and grain size to the driving force of the initial strain and the consequent stored energy as the samples with an initial small grain size have a higher number of nucleation sites during recrystallization than samples with a large initial grain size [18]. This means that

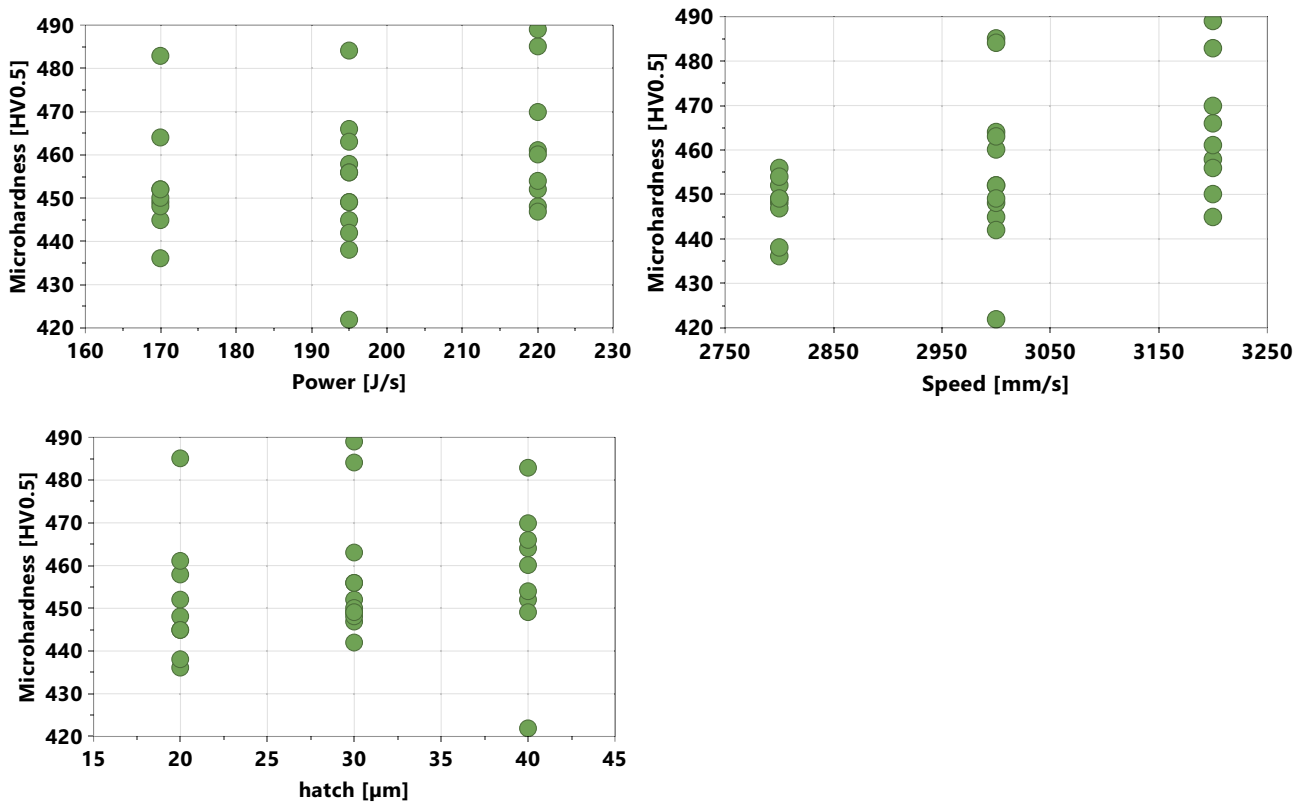


**Fig. 16.** Effect of the laser power, scanning speed, and hatch distance on the microhardness of the solution heat-treated samples. Although no marked effect was observed for laser power and hatch distance, the effect of the scanning speed was slightly noticeable.

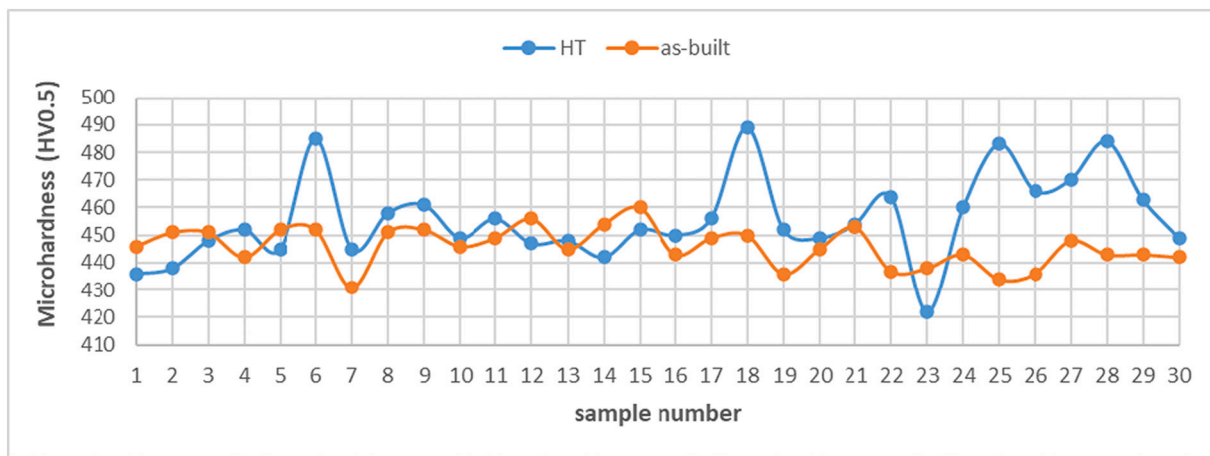


Fig. 17. Microhardness of the samples in the as-built (obtained from Ref. [6]) and heat-treated conditions (performed in this study).

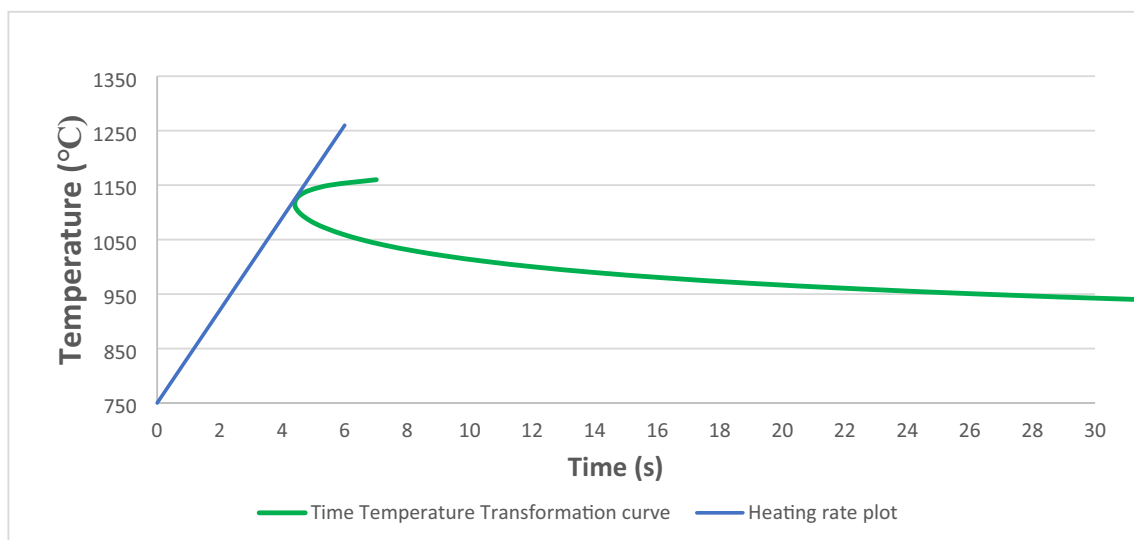


Fig. 18. TTT diagram for the  $\gamma'$  precipitate (15% volume fraction) modeled in JMatPro. The blue plot denotes the minimum heating rate required to avoid the precipitation of the  $\gamma'$  precipitate. (For interpretation of the references to colour in this figure legend, the reader is referred to the web version of this article.)

the recrystallization of grains may be driven more by nucleation than by growth. Thus, sample 22 with a small grain size in the as-built condition produced smaller grains in 22HT than 30HT, assuming that the amount of stored energy was approximately the same in the two samples 22 and 30. This reasoning indicates that sample 30HT should have a smaller grain size than sample 3HT. However, as discussed earlier, the initial plastic strain and stored energy also influence the final grain size. The plastic strains were not measured experimentally, thus it was not possible to evaluate the effect of the relationship between the initial plastic strains on the final heat-treated grain size. This analysis becomes complex when the texture is considered. It is well-known that the texture of plastically deformed materials before and after the deformation influences the recrystallization of their grains [18]. The texture analysis showed in Figs. 6 and 7 indicates that sample 22 had weaker  $\langle 001 \rangle$  texture than samples 3 and 30. This may have contributed to the difference in the final grain sizes of the samples. Texture was reduced in samples 3HT, 30HT, and 22HT. A reduction in the texture was also observed in a study performed by Engeli. This reduction in the texture enables a reduction in the anisotropy (high anisotropy in the as-built condition and low anisotropy in the heat-treated condition) of the material. The grain sizes of samples 1–30 in the as-built condition were observed using optical microscopy and SEM. The sizes were assessed

visually. The samples with small grain sizes in the as-built condition produced small grain sizes in the heat-treated condition. Thus, it appears that there is a correlation between the small grain sizes in the as-built and heat-treated conditions. Another possible factor influencing the heat-treated grain size is the effect of the second-phase particles, for example, bright spherical particles (carbides and/or oxides) and  $\gamma'$  precipitate. Second-phase particles may pin the grain boundaries to restrain the grain growth [18,20,22]. The possible influence of the  $\gamma'$  precipitate on the grain size of the heat-treated samples was evaluated by plotting the microhardness of the samples (in the as-built and heat-treated conditions) against the grain height and/or width after heat treatment. The findings did not indicate any significant correlation.

#### 4.3. $\gamma'$ dissolution, microhardness and homogenization

The  $\gamma'$  precipitate was detected after the solution heat treatment, followed by quenching. The L-PBF process parameters did not show strong effect on the heat-treated microhardness which suggested that the former had low influence on  $\gamma'$  strengthening. The microhardness values of many samples in the as-built and heat-treated conditions were similar. These microhardness values were also close to the microhardness values obtained after aging, as reported in Ref. [2,32]. A possible debate is

whether it is necessary to perform aging heat treatments when such high microhardness can be obtained by a solution heat treatment. Recall from Section 1 that Carter [9] recommended a solution heat treatment without subsequent aging heat treatment. The  $\gamma'$  precipitate was also observed after solution heat-treatment in a study performed by Divya et al. [11]. The microhardness obtained after the solution heat treatment was approximately 512 HV. The reason for the presence of the  $\gamma'$  precipitate after heating to 1260 °C and quenching may be the incomplete dissolution. This may also be because the  $\gamma'$  precipitate reprecipitated. It has been reported that the dissolved  $\gamma'$  precipitate reprecipitates after recrystallization [22,33]. Some of the  $\gamma'$  precipitate also formed during the cooling process. It was observed that the cells in the as-built condition (Fig. 3) disappeared after the solution heat treatment (Fig. 5). Homogenization followed the elimination of the cells and the dissolution of the  $\gamma/\gamma'$  eutectic. As discussed in Section 1, L-PBF Alloy 247LC was reported to homogenize after a solution heat treatment at 1260 °C for 2 h [34]. Homogenization was suspected to occur because neither cells nor microsegregation of elements between the cells was observed after the heat treatment, even though they were observed in the as-built condition. The first loop heating curve of sample 31 at a heating rate of 5 °C/s shown in Fig. 15a is a representative of the furnace heating rate used in this investigation. It has been reported that when directionally solidified CMSX-10 is solution heat-treated, the  $\gamma'$ , solidus, and liquidus temperatures shift to higher values, which can be attributed to the dissolution of  $\gamma/\gamma'$  and the subsequent homogenization [35]. The  $\gamma'$  temperature increases by 15 °C, the solidus temperature increases by 25 °C, and the liquidus temperature increases by 5 °C after the solution heat treatment of the aforementioned study. In the present study, the  $\gamma'$  and liquidus temperatures of 31HT were close to those of 31. The solidus could not be identified in the samples. The fact that  $\gamma'$  solvus did not increase in 31HT indicates that there was no significant post-homogenization increase in the  $\gamma'$  forming elements that promote such an increase. When the  $\gamma/\gamma'$  dissolves, as suggested from the microscopy observations here, it is accompanied by the release of high atomic number elements such as Ta, which diffuse into the dendrite core and subsequently partition to the  $\gamma'$  formed during cooling [35]. This may then increase the  $\gamma'$  solvus in the DSC experiment. Thus, the DSC results here could not be utilized to substantiate the microscopic observation of the dissolution of  $\gamma/\gamma'$  and the possible occurrence of homogenization. Further investigation is needed to analyze the microsegregation profile, which can be performed using atomic probe tomography. As shown in Fig. 15 and Tables 4a and 4b, the heating curve shifted to the right during the second loop heating along with an increase in the liquidus temperature. The first loop heating curve (Fig. 15a) shows the first cycle heating of the as-built L-PBF sample, which had a specific material condition and an amount of  $\gamma/\gamma'$ . Subsequently, at higher temperatures, the material melted, and the liquid so formed then solidified, as illustrated by the first loop cooling curve. A second cycle was then performed, as illustrated by the second heating and cooling loop. Note that the material being heated in the second loop was processed differently as compared to the as-built sample, which was heated in the first loop heating. As such, the composition and amount of  $\gamma/\gamma'$  differed. It is likely that a more homogenized composition in the second loop material promotes a higher liquidus.

## 5. Conclusion

The influence of the L-PBF process parameters on the microstructure of a solution heat-treated Alloy 247LC was investigated. The main conclusions are as follows.

- Cracking (likely strain-age cracking) was observed in the microstructure. It is estimated that a high heating rate of approximately 85 °C/s from 750 °C suppressed the precipitation of 15% volume fraction of the  $\gamma'$  precipitate. This is most likely to reduce the strain-age cracking.

- The L-PBF process parameters that influenced the grain size of the solution heat-treated alloy can be identified.
- Among all the process parameters investigated, the laser power affected the grain height and aspect ratio most significantly, while the interaction between the laser power and hatch distance was the most significant process parameter influencing the grain width.
- The as-built grain size of the investigated samples most likely influenced the recrystallization process. The smallest as-built grain-size produced the smallest heat-treated grain size.
- The material condition that resisted solidification cracking during L-PBF printing (sample 30), produced relatively large grains after solution-heat treatment (sample 30HT). The large grain size in this material condition possibly provides better creep resistance than the small grain size material conditions.
- Recrystallization occurred in the investigated samples printed with high, medium, and low energy densities.
- The strong <001> texture in high and medium energy densities in the as-built condition reduced as a result of the solution heat treatment.
- The L-PBF process parameters had a low influence on the  $\gamma'$  strengthening of the solution heat-treated material conditions.

## Data availability

The raw/processed data required to reproduce these findings cannot be shared at this time as the data also forms part of an ongoing study.

## Funding

This work was supported by KK foundation, Sweden through SUMAN Next and PODFAM projects (grant number 2016-0281).

## Declaration of Competing Interest

The authors declare that they have no known competing financial interests or personal relationships that could have appeared to influence the work reported in this paper.

## Acknowledgements

The authors thank Sneha Goel for calibrating the furnace and her leadership during the heat treatment process. The authors thank Chamara Kumara for his contributions during the planning of the DSC experiment.

## References

- [1] M.J. Donachie, S.J. Donachie, *Superalloys: A Technical Guide*, 2nd ed., ASM International, Materials Park, OH, 2002.
- [2] Y.T. Tang, et al., Alloys-by-design: application to new superalloys for additive manufacturing, *Acta Mater.* 202 (Jan 2021) 417–436, <https://doi.org/10.1016/j.actamat.2020.09.023>.
- [3] S. Griffiths, et al., Combining alloy and process modification for micro-crack mitigation in an additively manufactured Ni-base superalloy, *Addit. Manuf.* 36 (Dec 2020), 101443, <https://doi.org/10.1016/j.addma.2020.101443>.
- [4] M. Gerstgrasser, M. Cloots, J. Stirnimann, K. Wegener, Focus shift analysis, to manufacture dense and crack-free SLM-processed CM247LC samples, *J. Mater. Process. Technol.* 289 (Mar 2021), 116948, <https://doi.org/10.1016/j.jmatprotec.2020.116948>.
- [5] R. Engeli, Selective laser melting & heat treatment of  $\gamma'$  strengthened Ni-base superalloys for high temperature applications, ETH Zurich (2017), <https://doi.org/10.3929/ETHZ-B-000000074>.
- [6] O. Adegoke, J. Andersson, H. Brodin, R. Pederson, Influence of laser powder bed fusion process parameters on voids, cracks, and microhardness of nickel-based superalloy alloy 247LC, *Materials* 13 (17) (Aug 2020) 3770, <https://doi.org/10.3390/ma13173770>.
- [7] N. Kalentics, et al., Healing cracks in selective laser melting by 3D laser shock peening, *Addit. Manuf.* 30 (Dec 2019), 100881, <https://doi.org/10.1016/j.addma.2019.100881>.
- [8] S. Catchpole-Smith, N. Aboulkhair, L. Parry, C. Tuck, I.A. Ashcroft, A. Clare, Fractal scan strategies for selective laser melting of 'unweldable' nickel superalloys, *Addit. Manuf.* 15 (May 2017) 113–122, <https://doi.org/10.1016/j.addma.2017.02.002>.

- [9] L.N. Carter, *Selective Laser Melting of Nickel Superalloys for High Temperature Applications*, Ph.D, University of Birmingham, Birmingham, UK, 2013.
- [10] X. Wang, L.N. Carter, B. Pang, M.M. Attallah, M.H. Loretto, Microstructure and yield strength of SLM-fabricated CM247LC Ni-Superalloy, *Acta Mater.* 128 (Apr 2017) 87–95, <https://doi.org/10.1016/j.actamat.2017.02.007>.
- [11] V.D. Divya, et al., Microstructure of selective laser melted CM247LC nickel-based superalloy and its evolution through heat treatment, *Mater. Charact.* 114 (Apr 2016) 62–74, <https://doi.org/10.1016/j.matchar.2016.02.004>.
- [12] L.N. Carter, K. Essa, M.M. Attallah, Optimisation of selective laser melting for a high temperature Ni-superalloy, *Rapid Prototyp. J.* 21 (4) (Jun 2015) 423–432, <https://doi.org/10.1108/RPJ-06-2013-0063>.
- [13] M. Thomas, G.J. Baxter, I. Todd, Normalised model-based processing diagrams for additive layer manufacture of engineering alloys, *Acta Mater.* 108 (Apr 2016) 26–35, <https://doi.org/10.1016/j.actamat.2016.02.025>.
- [14] L.N. Carter, C. Martin, P.J. Withers, M.M. Attallah, The influence of the laser scan strategy on grain structure and cracking behaviour in SLM powder-bed fabricated nickel superalloy, *J. Alloys Compd.* 615 (Dec 2014) 338–347, <https://doi.org/10.1016/j.jallcom.2014.06.172>.
- [15] K. Harris, G.L. Erickson, R.E. Schwer, MAR M 247 derivations - CM 247 LC DS alloy and CMSX single crystal alloys: properties & performance, in: *Superalloys 1984* (fifth international symposium), 1984, pp. 221–230, [https://doi.org/10.7449/1984/Superalloys\\_1984\\_221\\_230](https://doi.org/10.7449/1984/Superalloys_1984_221_230).
- [16] H. Hilal, R. Lancaster, S. Jeffs, J. Boswell, D. Stapleton, G. Baxter, The influence of process parameters and build orientation on the creep behaviour of a laser powder bed fused Ni-based superalloy for aerospace applications, *Materials* 12 (9) (Apr 2019) 1390, <https://doi.org/10.3390/ma12091390>.
- [17] P. Fernandez-Zelaia, M.M. Kirka, A.M. Rossy, Y. Lee, S.N. Dryepont, Nickel-based superalloy single crystals fabricated via electron beam melting, *Acta Mater.* (Jun 2021) 117133, <https://doi.org/10.1016/j.actamat.2021.117133>.
- [18] F.J. Humphreys, M. Hatherly, *Recrystallization and Related Annealing Phenomena*, 2nd ed., Elsevier, Amsterdam; Boston, 2004.
- [19] E. Chauvet, et al., Hot cracking mechanism affecting a non-weldable Ni-based superalloy produced by selective electron beam melting, *Acta Mater.* 142 (Jan 2018) 82–94, <https://doi.org/10.1016/j.actamat.2017.09.047>.
- [20] A. Ariasetta, S. Kobayashi, M. Takeyama, Y. Wang, S. Imano, Characterization of recrystallization and second-phase particles in solution-treated additively manufactured alloy 718, *Metall. Mater. Trans. A* 51 (2) (Feb 2020) 973–981, <https://doi.org/10.1007/s11661-019-05560-y>.
- [21] J.H. Boswell, D. Clark, W. Li, M.M. Attallah, Cracking during thermal post-processing of laser powder bed fabricated CM247LC Ni-superalloy, *Mater. Des.* 174 (Jul 2019), 107793, <https://doi.org/10.1016/j.matdes.2019.107793>.
- [22] R. Muñoz-Moreno, et al., Effect of heat treatment on the microstructure, texture and elastic anisotropy of the nickel-based superalloy CM247LC processed by selective laser melting, *Mater. Sci. Eng. A* 674 (Sep 2016) 529–539, <https://doi.org/10.1016/j.msea.2016.06.075>.
- [23] J. Xu, et al., *Alloy Design and Characterization of  $\gamma'$  Strengthened Nickel-Based Superalloys for Additive Manufacturing*, 2021.
- [24] A. Leicht, U. Klement, E. Hryha, Effect of build geometry on the microstructural development of 316L parts produced by additive manufacturing, *Mater. Charact.* 143 (Sep 2018) 137–143, <https://doi.org/10.1016/j.matchar.2018.04.040>.
- [25] C.T. Sims, N.S. Stoloff, W.C. Hagel (Eds.), *Superalloys II*, Wiley, New York, 1987.
- [26] N. Allain-Bonasso, F. Wagner, S. Berbenni, D.P. Field, A study of the heterogeneity of plastic deformation in IF steel by EBSD, *Mater. Sci. Eng. A* 548 (Jun 2012) 56–63, <https://doi.org/10.1016/j.msea.2012.03.068>.
- [27] A. Ayad, N. Allain-Bonasso, N. Rouag, F. Wagner, Grain orientation spread values in if steels after plastic deformation and recrystallization, *Mater. Sci. Forum* 702–703 (Dec 2011) 269–272, <https://doi.org/10.4028/www.scientific.net/MSF.702-703.269>.
- [28] S.I. Wright, M.M. Nowell, D.P. Field, A review of strain analysis using electron backscatter diffraction, *Microsc. Microanal.* 17 (3) (Jun 2011) 316–329, <https://doi.org/10.1017/S1431927611000055>.
- [29] H. Gruber, *Powder Bed Fusion Processing of Ni-Based Superalloys: Defect Formation and its Mitigation*, Chalmers University of Technology, 2020.
- [30] J.C. Lippold, *Welding Metallurgy and Weldability*, John Wiley & Sons Inc, Hoboken, New Jersey, 2015.
- [31] J.-H. Liao, H.-Y. Bor, C.-N. Wei, C.-G. Chao, T.-F. Liu, Influence of microstructure and its evolution on the mechanical behavior of modified MAR-M247 fine-grain superalloys at 871°C, *Mater. Sci. Eng. A* 539 (Mar 2012) 93–100, <https://doi.org/10.1016/j.msea.2012.01.059>.
- [32] O. Adegoke, J. Andersson, H. Brodin, O. Ojo, R. Pederson, Laser beam powder bed fusion and post processing of alloy 247LC, in: *Contributed papers from MS&T19*, 2019, pp. 27–34, [https://doi.org/10.7449/2019/MST\\_2019\\_27\\_34](https://doi.org/10.7449/2019/MST_2019_27_34).
- [33] A. Porter, B. Ralph, The recrystallization of nickel-base superalloys, *J. Mater. Sci.* 16 (3) (Mar 1981) 707–713, <https://doi.org/10.1007/BF02402788>.
- [34] S. Griffiths, et al., Influence of Hf on the heat treatment response of additively manufactured Ni-base superalloy CM247LC, *Mater. Charact.* 171 (Jan 2021), 110815, <https://doi.org/10.1016/j.matchar.2020.110815>.
- [35] G.E. Fuchs, Solution heat treatment response of a third generation single crystal Ni-base superalloy, *Mater. Sci. Eng. A* 300 (1–2) (Feb 2001) 52–60, [https://doi.org/10.1016/S0921-5093\(00\)01776-7](https://doi.org/10.1016/S0921-5093(00)01776-7).